JOURNAL OF THERMOPHYSICS AND HEAT TRANSFER
Vol. 6, No. 2, April–June 1992

Transient Behavior of Axially Grooved Heat Pipes with Thermal Energy Storage

Ming-Jr Chang* and Louis C. Chow†
University of Kentucky, Lexington, Kentucky 40506
and
Won Soon Chang‡ and Micheal J. Morgan§
Wright Research and Development Center, Wright-Patterson Air Force Base, Ohio 45433

A novel design of a high-temperature axially grooved heat pipe (HP) incorporated with thermal energy storage (TES) to mitigate pulse heat loads are presented. The transient behavior of the HP/TES device was simulated using a three-dimensional numerical model based on finite-difference approximations. A phase-change material (PCM) encapsulated in cylindrical containers was used as thermal energy storage. The transient response of three different HP/TES configurations were compared: 1) heat pipe with one big empty cylinder installed in the vapor core, 2) heat pipe with one big PCM cylinder, and 3) heat pipe with six small PCM cylinders. From the numerical results, it was found that the PCM is very effective in mitigating the adverse effect of pulse heat loads on normal heat pipe operation.

Nomenclature

c = specific heat
D_h = hydraulic diameter of vapor flow
f = vapor friction coefficient or f factor
H = enthalpy
k = thermal conductivity
l_c = length of condensation region
Ma = Mach number
$\dot{m}$ = axial local vapor mass rate
P = vapor pressure
Re = axial Reynolds number of vapor flow
Re_w = radial Reynolds number of vapor flow
r, θ, z = space coordinates
Ste = Stefan number of phase-change material
T = temperature
t = time
$\bar{U}$ = mean axial vapor velocity
v = radial vapor velocity
α = thermal diffusivity
γ = ratio of specific heats
δ^2 = central difference operator
ρ = density
τ = dimensionless time

Subscripts
i, j, k = nodal point indices in r, θ, and z directions
L = laminar flow
l = liquid state
s = solid state
T = turbulent flow
t = thermal energy storage

Superscript
n = time index

Introduction

FUTURE space missions will involve thermal transport devices with ability to handle transient heat loads, especially those with a high peak-to-average (p/a) power ratio. Conventional heat pipe (HP) designs work well with transient heat loads with low p/a power ratios. Incorporation of thermal energy storage (TES) into a heat pipe/heat rejection system is a promising method to mitigate the high p/a power ratio heat loads. Some configurations for the mitigation of heat loads has been proposed by Beam[1] and Sheffield[2] but detailed analyses of these HP/TES mitigation techniques had not been attempted. These concepts must be tested and understood so that they may be integrated successfully into an overall thermal control system design.

A modified three-dimensional (3-D) alternating-direction implicit (ADI) finite-difference method developed by the authors[3] was used to model the heat conduction through the wall and wicks, including the liquid in the grooves. This modification allows the time step to be increased by about two orders of magnitude without compromising significantly on the accuracy of the numerical solution. It was also found that this modified ADI method yields much higher accuracy than the well-known Douglas's and Brian's ADI methods.[4,5]

The vapor flow was modeled by Bowman[6] using a quasi-steady one-dimensional friction coefficient. The vapor flow models developed by Hall and Doster,[7] Kelly and Schor,[8] and Issacci et al.[9] are clearly superior. However, their calculations require prohibitively large computational times. Bowman[6] made a very important conclusion that since the response time of the vapor dynamics is very short compared to the heat transfer response time of the heat pipe wall and wick, the vapor flow can be modeled as a quasisteady process. He also studied the compressible vapor dynamics in a heat pipe experimentally using air flowing in a porous tube with blowing and suction along the wall. He modeled the vapor flow using a numerical solution to the axisymmetric, unsteady Navier-Stokes equations and a steady one-dimensional solution technique. He concluded that it is adequate to treat the vapor flow as one-dimensional and has also provided suitable vapor pressure drop correlations.

In the numerical solution of heat conduction problems with phase change (Stefan's problem) by finite differences, en-

Presented as Paper 90-1754 at the AIAA/ASME 5th Joint Thermophysics and Heat Transfer Conference, Seattle, WA, June 18–20, 1990; received July 16, 1990; revision received Jan. 15, 1991; accepted for publication Feb. 2, 1991.

*Graduate Student, Mechanical Engineering Department.
†Professor, Mechanical Engineering Department. Senior Member AIAA.
‡Senior Research Scientist, Aero Propulsion and Power Laboratory.
§Engineer, Aero Propulsion and Power Laboratory.

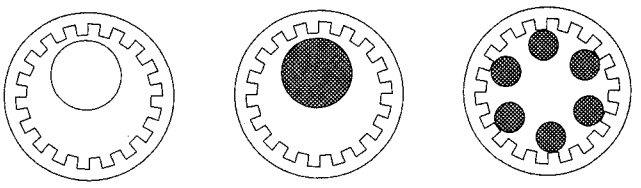

Fig. 1 Three different HP/TES configurations.

thalpy methods or heat capacity methods can be used. The former methods require either an explicit procedure, which may lead to convergence problems, or iteration at each time step if an implicit procedure is used. The latter methods have the problem of jumping the latent heat peak, necessitating the use of very small time steps to avoid underprediction of the phase-change time. Recently, Hsiao[10] proposed a new finite-difference method for the Stefan's problem. In his scheme, the equivalent heat capacity at a node is a function of the temperature at that node and all the surrounding nodes. Hsiao concluded that his method can avoid the problem of jumping the latent heat peak and allows the use of a relatively large time step. Hsiao's method was tested, but a large energy balance error was found. Pham[11,12] suggested a simple method that combines the enthalpy methods and heat capacity methods. Comparing this method with the other existing methods for test problems with exact solutions, Pham pointed out that most of the methods agree to within 0.2% with the analytical results, except for Hsiao's method, which yielded results with up to 22% error. The low accuracy of the Hsiao's method could be due to its ambiguous theoretical basis. Pham also concluded that his method is much faster than the other methods. However, Pham's method has a singularity problem in finding the equivalent specific heat. In this paper, we adopted the good features of Pham's method with some modifications. The modified Pham's method for solving melting and solidification problems was checked against a test problem with an exact solution. It was found that the modified Pham's method yields accurate numerical results and does not have the singularity problem of the original Pham's method.

In this paper, a stainless steel grooved heat pipe using sodium as the working fluid was modeled. The grooved heat pipe has been used quite successfully. However, the rather large nominal diameter of the grooves makes the capillary limit very low. Barantsevich et al.[13] showed experimentally that if the grooves are wrapped with layers of fine wick mesh, the capillary limit can be improved significantly while maintaining low liquid flow resistance.

We applied our numerical model (described below) to several l-m-long heat pipes. Three different HP/TES configurations as shown in Fig. 1 were investigated with several types of pulse heat loads. It was found that the use of a phase-change material (PCM) as thermal energy storage is a very effective method of mitigating the adverse effect of pulse heat loads on normal heat pipe operation. If the peak heat load stops before all the PCM has been completely melted, the temperature change of the heat pipes with PCM is insignificant. The modified 3-D ADI finite difference method can predict the transient heat conduction behavior very well. We have checked the total energy balance and find the error is less than 1% at each time step.

Numerical Model

The pipe wall and wick, including the liquid in the grooves were modeled as three-dimensional in the radial, angular, and axial directions. We assumed that the heat transferred through the wick and working fluid is by conduction only because liquid flow velocity is very low and the liquid thermal conductivitiy is very high. Also, it was assumed that the grooves are nearly filled with liquid. This is a good assumption for high-temperature heat pipes under normal operation without burnout because the thermal resistance of liquid metal is much smaller than that of the heat pipe wall. The vapor flow was modeled using a quasisteady one-dimensional friction coefficient model. Because the thermal resistance of the condensed liquid on the TES is much smaller than that of the PCM, the surface temperature of the TES is assumed to be equal to the vapor temperature at the same axial location. Hence, if the PCM is encapsulated in a cylindrical container, only a two-dimensional analysis is needed to calculate the temperature and heat transfer within the PCM, because of angular symmetry.

Pipe Wall and Wick

The improved three-dimensional ADI finite-difference method[3] was used to model the heat conduction through the wall and wick, including the liquid in the grooves. The advantage of the ADI method is that only tridiagonal matrices need to be solved. However, the conventional three-dimensional ADI method is conditionally stable and very small time-steps are required to ensure convergence and stability. Because small Δr is needed due to the slender geometry of the heat pipe, only very small Δt (about 0.001 s) can be used with the conventional ADI method. Other forms of the ADI method include Douglas's method[4] and Brian's method.[5] Douglas's and Brian's ADI methods are unconditionally stable, they possess the advantages of the implicit scheme with no limitation on the size of the time step. However, Thibault[14] pointed out that these two unconditionally stable ADI methods cannot retain good accuracy if the time step is more than two times larger than the time-step limit required for the conventional ADI method. The conventional ADI method was modified by introducing an f factor ($0 < f < 1$).[3] This modification allows the time step to be increased by about two orders of magnitude without compromising significantly on the accuracy of the numerical solution. It was also shown that this new ADI method yields much higher accuracy than Brian's and Douglas's ADI methods.

The conventional, Douglas's and Brian's ADI methods have a comon problem: negative coefficients in their discretization equations that are physically unrealistic.[15] After the three-dimensional finite-difference equations of the conventional ADI method in cylindrical coordinates are modified by an f factor, they become the following equations:

$$\frac{1}{\alpha}\frac{T^{n+1/3}_{i,j,k} - T^{n}_{i,j,k}}{\Delta t/3} = (3 - 2\mathbf{f})\delta_r^2 T^{n+1/3}_{i,j,k} + \mathbf{f}\delta_\theta^2 T^{n}_{i,j,k} + \mathbf{f}\delta_z^2 T^{n}_{i,j,k} \tag{1}$$

$$\frac{1}{\alpha}\frac{T^{n+2/3}_{i,j,k} - T^{n+1/3}_{i,j,k}}{\Delta t/3} = \mathbf{f}\delta_r^2 T^{n+1/3}_{i,j,k} + (3 - 2\mathbf{f})\delta_\theta^2 T^{n+2/3}_{i,j,k} + \mathbf{f}\delta_z^2 T^{n+1/3}_{i,j,k} \tag{2}$$

$$\frac{1}{\alpha}\frac{T^{n+1}_{i,j,k} - T^{n+2/3}_{i,j,k}}{\Delta t/3} = \mathbf{f}\delta_r^2 T^{n+2/3}_{i,j,k} + \mathbf{f}\delta_\theta^2 T^{n+2/3}_{i,j,k} + (3 - 2\mathbf{f})\delta_z^2 T^{n+1}_{i,j,k} \tag{3}$$

After rearranging Eqs. (1–3), the following discretization equations can be obtained:

$$\left[\frac{3\rho c r_i(\Delta r)^2}{\Delta t} + (3 - 2\mathbf{f})k_{i-}\left(r_i + \frac{\Delta r}{2}\right) + (3 - 2\mathbf{f})k_{i+}\left(r_i - \frac{\Delta r}{2}\right)\right] T^{n+1/3}_{i,j,k} - (3 - 2\mathbf{f})k_{i-}\left(r_i + \frac{\Delta r}{2}\right) T^{n+1/3}_{i-1,j,k} - (3 - 2\mathbf{f})k_{i+}\left(r_i - \frac{\Delta r}{2}\right) T^{n+1/3}_{i+1,j,k}$$

$$= \left[\frac{3\rho c r_i(\Delta r)^2}{\Delta t} - \mathbf{f}(k_{j-} + k_{j+})\frac{(\Delta r)^2}{r_i(\Delta\theta)^2} - \mathbf{f}(k_{k-} + k_{k+})\frac{r_i(\Delta r)^2}{(\Delta z)^2}\right] T^n_{i,j,k} + \left[\mathbf{f}k_{j-}\frac{(\Delta r)^2}{r_i(\Delta\theta)^2}\right] T^n_{i,j-1,k} + \left[\mathbf{f}k_{j+}\frac{(\Delta r)^2}{r_i(\Delta\theta)^2}\right] T^n_{i,j+1,k} + \left[\mathbf{f}k_{k+}\frac{r_i(\Delta r)^2}{(\Delta z)^2}\right] T^n_{i,j,k-1} + \left[\mathbf{f}k_{k+}\frac{r_i(\Delta r)^2}{(\Delta z)^2}\right] T^n_{i,j,k+1} \quad (4)$$

$$\left[\frac{3\rho c(r_i\Delta\theta)^2}{\Delta t} + (3 - 2\mathbf{f})k_{j-} + (3 - 2\mathbf{f})k_{j+}\right] \cdot T^{n+2/3}_{i,j,k} - (3 - 2\mathbf{f})k_{j-}T^{n+2/3}_{i,j-1,k} - (3 - 2\mathbf{f})k_{j+}T^{n+2/3}_{i,j+1,k} = \left[\frac{3\rho c(r_i\Delta\theta)^2}{\Delta t} - \mathbf{f}k_{i-}\left(r_i + \frac{\Delta r}{2}\right)\frac{r_i(\Delta\theta)^2}{(\Delta r)^2} - \mathbf{f}k_{i+}\left(r_i - \frac{\Delta r}{2}\right)\frac{r_i(\Delta\theta)^2}{(\Delta r)^2} - \mathbf{f}(k_{k-} + k_{k+})\frac{(r_i\Delta\theta)^2}{(\Delta z)^2}\right] T^{n+1/3}_{i,j,k} + \left[\mathbf{f}k_{i-}\left(r_i + \frac{\Delta r}{2}\right)\frac{r_i(\Delta\theta)^2}{(\Delta r)^2}\right] T^{n+1/3}_{i-1,j,k} + \left[\mathbf{f}k_{i+}\left(r_i - \frac{\Delta r}{2}\right)\frac{r_i(\Delta\theta)^2}{(\Delta r)^2}\right] T^{n+1/3}_{i+1,j,k} + \left[\mathbf{f}k_{k-}\frac{(r_i\Delta\theta)^2}{(\Delta z)^2}\right] T^{n+1/3}_{i,j,k-1} + \left[\mathbf{f}k_{k+}\frac{(r_i\Delta\theta)^2}{(\Delta z)^2}\right] T^{n+1/3}_{i,j,k+1} \quad (5)$$

$$\left[\frac{3\rho c(\Delta z)^2}{\Delta t} + (3 - 2\mathbf{f})(k_{k-} + k_{k+})\right] T^{n+1}_{i,j,k} - (3 - 2\mathbf{f})k_{k-}T^{n+1}_{i,j,k-1} - (3 - 2\mathbf{f})k_{k+}T^{n+1}_{i,j,k+1} = \left[\frac{3\rho c(\Delta z)^2}{\Delta t} - \mathbf{f}k_{i-}\left(r_i + \frac{\Delta r}{2}\right)\frac{(\Delta z)^2}{r_i(\Delta r)^2} - \mathbf{f}k_{i+} \cdot \left(r_i - \frac{\Delta r}{2}\right)\frac{(\Delta z)^2}{r_i(\Delta r)^2} - \mathbf{f}(k_{j-} + k_{j+})\frac{(\Delta z)^2}{(r_i\Delta\theta)^2}\right] T^{n+2/3}_{i,j,k} + \left[\mathbf{f}k_{i-}\left(r_i + \frac{\Delta r}{2}\right)\frac{(\Delta z)^2}{r_i(\Delta r)^2}\right] T^{n+2/3}_{i-1,j,k} + \left[\mathbf{f}k_{i+}\left(r_i - \frac{\Delta r}{2}\right)\frac{(\Delta z)^2}{r_i(\Delta r)^2}\right] T^{n+2/3}_{i+1,j,k} + \left[\mathbf{f}k_{j-}\frac{(\Delta z)^2}{(r_i\Delta\theta)^2}\right] T^{n+2/3}_{i,j-1,k} + \left[\mathbf{f}k_{j+}\frac{(\Delta z)^2}{(r_i\Delta\theta)^2}\right] T^{n+2/3}_{i,j+1,k} \quad (6)$$

On the right-hand sides of Eqs. (4–6), only the coefficients for central nodal temperatures at previous time step could be negative. It was shown[3] that the time-step limit to avoid the coefficients from becoming negative can now be increased by a factor $1/f$. It was also shown[3] that the stability criterion can be increased by the same factor. So, it is clear that the time-step limit for the conventional ADI method can now be increased by a factor $1/f$ by using this new ADI method. The computational results showed that this modification allows the time-limit to be increased by two orders of magnitude with $f = 0.01$ and the solutions still remain stable with very high accuracy.

Melting and Solidification of PCM

Because the thermal resistance of the condensed liquid on the TES is much smaller than that of the phase-change material, the surface temperature of the TES is assumed to be equal to the vapor temperature at the same axial location. Hence, if the PCM is encapsulated in a cylindrical container, only a two-dimensional analysis is needed to calculate the temperature and heat transfer within the PCM because of angular symmetry.

Pham's method[11,12] can be used in conjunction with the two-dimensional ADI scheme with the following procedure:

1) At the start of each time step, the enthalpy change ΔH^* at each node is estimated from the known temperature $T^n_{i,k}$ of that node and those of its immediate neighbors at the old time step.

2) The estimated new temperature $T^*_{i,k}$ is calculated from the estimated new enthalpy $H^n_{i,k} + \Delta H^*$. The equivalent specific heat of that node is then defined as

$$c^*_{i,k} = \frac{\Delta H^*}{T^*_{i,k} - T^n_{i,k}} \quad (7)$$

3) With $c^*_{i,k}$ known, we can use the 2-D ADI method to find the new temperature $T^{n+1}_{i,k}$.

One of the good features of Pham's method is that it estimates the new temperature from the estimated enthalpy change to avoid the problem of jumping the latent heat peak. Another good feature of Pham's method is that its theoretical basis is clear. However, Pham's method may have a singularity problem in finding the equivalent specific heat in step 2. If there is no enthalpy change in a particular node, the estimated new temperature $T^*_{i,k}$ will be equal to the old temperature $T^n_{i,k}$. Then, we are not able to find the equivalent specific heat from Eq. (7). Fortunately, we have found a way around this problem. If we assume the melting temperature is T_m and the latent heat effect is over a $2\Delta T_m$ interval, and let $H_1 = f_H(T_m - \Delta T_m)$, $H_2 = f_H(T_m + \Delta T_m)$ and $H^{n+1}_{i,k} = H^n_{i,k} + \Delta H^*$, we can avoid the singularity problem by redefining the equivalent specific heat in Eq. (7) as follows:

$$c^*_{i,k} = \begin{cases} c_s & \text{if } H^n_{i,k}, H^{n+1}_{i,k} < H_1 \\ (H_2 - H_1)/(2\Delta T_m) & \text{if } H_1 < H^n_{i,k}, H^{n+1}_{i,k} < H_2 \\ c_l & \text{if } H^n_{i,k}, H^{n+1}_{i,k} > H_2 \\ \dfrac{\Delta H^*}{T^*_{i,k} - T^n_{i,k}} & \text{if } H^n_{i,k} < H_1 < H^{n+1}_{i,k} \\ & \text{or } H^n_{i,k} < H_2 < H^{n+1}_{i,k} \\ & \text{or } H^n_{i,k} > H_1 > H^{n+1}_{i,k} \\ & \text{or } H^n_{i,k} > H_2 > H^{n+1}_{i,k} \end{cases} \quad (8)$$

where c_s and c_l are the specific heats for solid state and liquid state.

After the modification, Eq. (7) is now used when only one of $H^n_{i,k}$ or $H^{n+1}_{i,k}$ falls in between H_1 and H_2. In other words, Eq. (7) can only be used when ΔH^* is not equal to zero. This modification avoids the singularity problem that Pham's method has.

Consider a one-dimensional melting problem with a solid in a half-space initially at the melting temperature $T_i = T_m = 950$ K. At time zero, the temperature at the front surface of the solid is suddenly heated to a constant temperature $T_0 = 1300$ K and melting takes place immediately. Figure 2 shows a comparison of temperature between the exact solu-

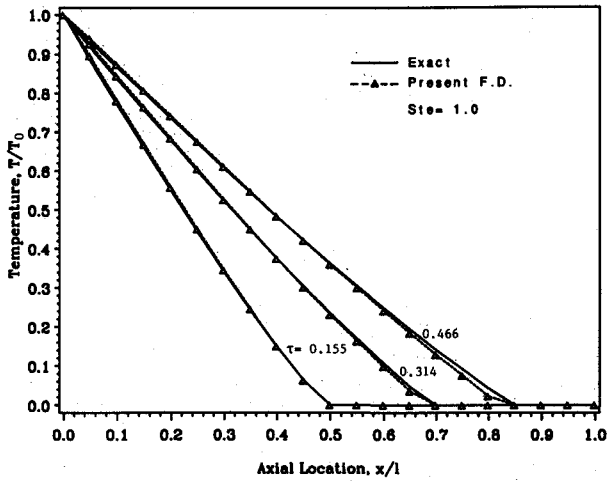

Fig. 2 Temperature distribution during melting of a one-dimensional half-space (*Ste* = 1).

tion and the present finite-difference solution during the melting process. The thermophysical properties chosen in the numerical experiment are: k_s = 4.2 W/m-K, k_l = 2.1 W/m-K; c_s = 6280 J/K-kg, c_l = 7370 J/K-kg, ρ_s = 690 kg/m^3, ρ_l = 550 kg/m^3, PCM latent heat L is 2.58 × 10^6 J/kg. These properties correspond to those of lithium hydride.[16] The finite-difference solution is obtained by using 100 equally spaced elements along a length l = 0.01 m. A time step Δt = 0.01 s and a phase transition temperature interval $2\Delta T_m$ = 2.0 K are used for this example. The dimensionless time is defined as $\tau = t/(1^2/\alpha_l)$. The Stefan number is defined as $Ste = c_l(T_0 - T_i)/L$ and is equal to unity in this problem. As it can be seen in Fig. 2, the present solution agrees very well with the exact solution.

One-Dimensional Vapor Flow Model

The vapor flow was modeled by using a quasisteady one-dimensional friction coefficient developed by Bowman.[6] In the evaporation region, mass blowing causes a slight steepening in the velocity gradients at the pipe wall, resulting in an increase in the vapor friction coefficient. The favorable pressure gradient in the mass blowing region causes the flow to remain laminar, even for very large axial Reynolds numbers. The correlation of the vapor friction coefficient in this region can be expressed as

$$f_L = \frac{16}{Re}(1.2337 - 0.2337e^{0.0363Re_w})e^{6Ma^{2/5}} \tag{9}$$

where Ma is the Mach number based on the local mean axial velocity $\bar{U}$, Re_w is the radial Reynolds number, and Re is the axial Reynolds number defined as

$$Re_w = \frac{\rho v D_h}{\mu}, \qquad Re = \frac{\rho \bar{U} D_h}{\mu}$$

ρ is the vapor flow density, μ is vapor dynamic viscosity, v is the radial velocity at the wall and D_h is the hydraulic diameter of the vapor core.

The friction coefficient for fully developed turbulent flow with mass suction in the condensation region can be expressed as

$$f_T = \frac{0.046}{Re^{1/5}}\left[1 + 55Re^{0.1}\left(\frac{v}{\bar{U}}\right)^{0.9}\left(\frac{2l_c}{D_h}\right)^{0.1} e^{6Ma^{2/5}}\right] \tag{10}$$

where 1_c is the length of the condensation region.

For the transition region where the vapor flow is transitioning from laminar to turbulent and from a region of blowing to a region of suction. The correlation of the friction coefficient can be expressed as

$$f = f_T + (f_L - f_T)e^{-0.412\bar{z}^2} \tag{11}$$

where $\bar{z} = [(z - z_{t,i})/0.25\text{ m}]$, $z_{t,i}$ denotes the initial location of the transition region, and 0.25 m is a length determined empirically by Bowman.[6]

The vapor flow was assumed to be compressible, one-dimensional, and quasisteady. The form of the equations employing influence coefficients presented by Shapiro[17] was used

$$\frac{dMa^2}{Ma^2} = F_{f,a}4f\frac{dz}{D_h} + F_{\dot{m},a}\frac{d\dot{m}}{\dot{m}} \tag{12}$$

where the influence coefficients are defined as

$$F_{f,a} = \frac{4Ma^2\left[1 + \dfrac{\gamma - 1}{2}Ma^2\right]}{1 - Ma^2} \tag{13}$$

$$F_{\dot{m},a} = \frac{2[1 + \gamma Ma^2]\left[1 + \dfrac{\gamma - 1}{2}Ma^2\right]}{1 - Ma^2} \tag{14}$$

f is a friction coefficient defined earlier by Eqs.(9–11), γ is the ratio of specific heats, z is the axial coordinate, and $\dot{m}$ is the mass flow rate.

A second expression was needed to relate the change in total pressure (P_0) to the change in mass flow rate and to the friction coefficient. From Shapiro[17]

$$\frac{dP_0}{P_0} = F_{f,b}4f\frac{dz}{D_h} + F_{\dot{m},b}\frac{d\dot{m}}{\dot{m}} \tag{15}$$

where

$$F_{f,b} = \frac{-\gamma Ma^2}{2} \tag{16}$$

$$F_{\dot{m},b} = -\gamma Ma^2 \tag{17}$$

Other relations used are

$$\frac{T_a}{T_b} = \frac{1 + \dfrac{\gamma - 1}{2}Ma_b^2}{1 + \dfrac{\gamma - 1}{2}Ma_a^2} \tag{18}$$

$$\frac{P_b}{P_a} = \frac{(P_0)_b}{(P_0)_a}\left[\frac{T_a}{T_b}\right]^{\gamma/\gamma - 1} \tag{19}$$

$$\frac{\rho_a}{\rho_b} = \frac{P_a T_b}{P_b T_a} \tag{20}$$

These relate properties between two different axial locations a and b in the vapor flow field.

To calculate the pressure and temperature variations in the vapor flow, we need to know the evaporation and condensation rates. However, these rates depend on the vapor temperature and liquid-vapor interface temperature distributions. This means that the vapor pressure and temperature variations are coupled to evaporation and condensation rates simultaneously. In the present model, the evaporation and condensation rates are coupled to the vapor temperature and pressure in an explicit manner so that no iterations are required. However, we still have to guess the vapor temperature at the evaporator end in order to calculate the vapor tem-

perature distribution. The vapor temperature at the evaporator end can be estimated based on an assumption. Because the vapor density is very small, we can assume that the heat absorbed by the vapor itself is negligible compared to the evaporation and condensation rates. In other words, at every time step, the evaporation rate and the condensation rate are equal.

Results and Discussions

We applied the present numerical model to a heat pipe with 18 grooves using sodium as the working fluid. Materials for the heat pipe container are type 316 stainless steel. The total length of heat pipe is 1.0 m and the lengths of the evaporator, condenser, and adiabatic sections are 0.3 m, 0.3 m and 0.4 m, respectively. The heat pipe outside diameter is 1.9 cm ($\frac{3}{4}$ in.) and the inside diameter is 1.4 cm. Uniform heat flux is applied to the evaporator and heat is removed at the condenser by radioactive heat transfer to the ambient, which is maintained at 0 K. The emissivity of the condenser wall surface is assumed equal to unity. Lithium hydride is used as the phase change material (PCM). The latent heat is 2.58×10^6 J/kg and the melting temperature is 956 K.

For the numerical modeling of the heat pipe wall and wick, eight and forty nodes were chosen in the radial and axial directions, and only four nodes in the angular direction for a groove unit. The transient response of three different HP/TES configurations were compared: 1) heat pipe with one big empty cylinder installed in the vapor core, 2) heat pipe with one big PCM cylinder, and 3) heat pipe with six small PCM cylinders. The radii of the big and small cylinders are 0.4 and 0.163 cm, respectively. The big PCM cylinder has the same amount of PCM that the six small PCM cylinders have. The vapor hydraulic diameters are about 0.82 cm for the heat pipe with one big PCM cylinder and about 0.75 cm for the one with six small PCM cylinders. For the numerical modeling of PCM, 40 nodes in radial direction were chosen for big PCM and 16 nodes for small ones. The phase-transition temperature interval $2\Delta T_m = 10$ K was assumed and the time step $\Delta t = 0.1$ s was used for all the examples in this paper.

Figure 3 shows the transient response of three different HP/TES configurations with a higher heat load suddenly applied to the evaporator. Before $t = 10$ s, all three different heat pipes are operating at steady-state under a uniform heat load $q = 4.3$ W/cm² at the evaporator. The average heat pipe temperature is about 940 K. At $t = 10$ s, a higher heat load of $q = 10$ W/cm² is suddenly applied to the evaporator. As we can see, the temperature of the heat pipe without PCM increases very rapidly. The temperatures of the other two heat pipes with PCMs also increase rapidly right after the higher heat loads are applied, but the rapid temperature increases are arrested after the PCMs reach the melting temperature and start to melt. It can also be seen that the temperature increase of the heat pipe with six small PCMs is much slower than the other one with one big PCM during the melting process. This is because the total heat transfer surface area of the six small PCMs is larger and the heat conduction path is shorter compared to the case with one big PCM. However, the six small PCMs are completely melted earlier than the one big PCM. The six small PCMs are completely melted at about $t = 100$ s and the one big PCM is completely melted at about $t = 130$ s. After the PCMs are completely melted, the temperature of both heat pipes with PCMs starts to increase rapidly and the heat pipes reach a new steady-state condition with $q = 10$ W/cm². The heat pipe without PCM reaches the new steady-state condition at about $t = 350$ s, the other two heat pipes with PCM reach the steady-state condition later at about $t = 580$ s.

Figure 4 shows the axial variation of vapor pressure and temperature of three different HP/TES configurations at $t = 100$ s. The heat pipe without PCM has a vapor temperature of 1082 K, which is much higher than those of the other two heat pipes with PCM. The heat pipe with one big PCM has a vapor temperature of 985 K and the one with six small PCMs has a vapor temperature of only 968 K. The results in Fig. 4 show that the vapor pressure and temperature drops are strongly dependent on the operating vapor temperature. A lower vapor temperature will result in a lower vapor sound speed and a higher Mach number. From Eqs. (9–11) we can see that higher Mach numbers lead to higher friction coefficients, resulting in larger total pressure drops. The higher Mach numbers also cause the static pressure to drop even more. In the adiabatic section, there is much less mass blowing or suction.

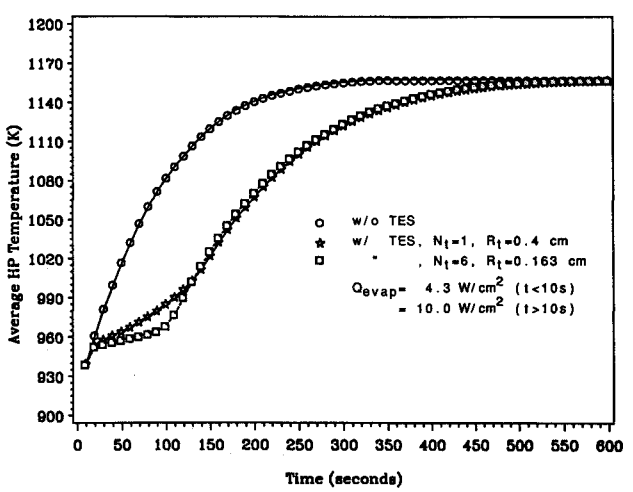

Fig. 3 Transient response of heat pipes with a sudden increase in heat input.

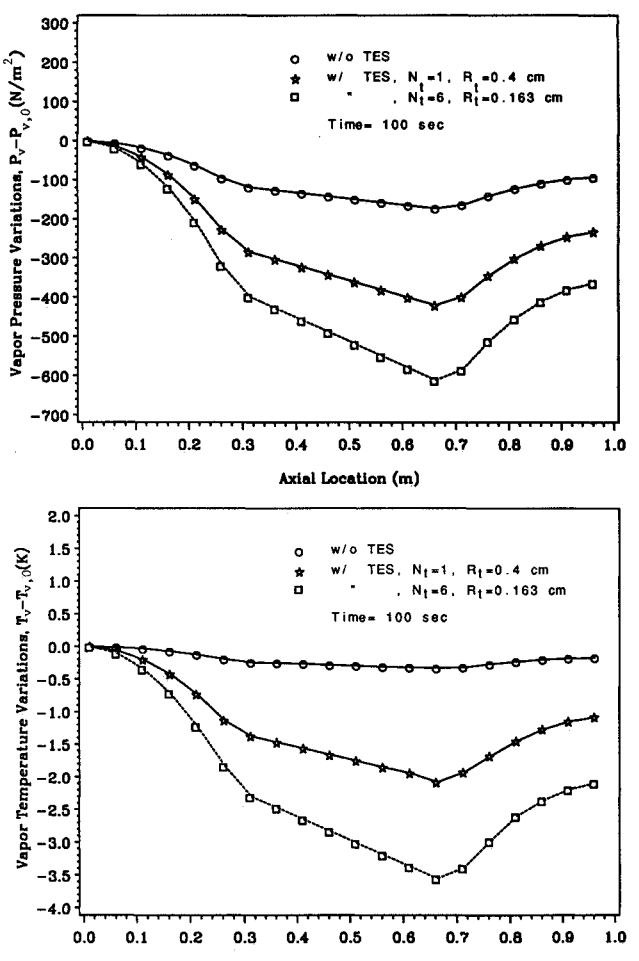

Fig. 4 Axial variations of vapor pressure and temperature at $t = 100$ s.

Hence, the pressure decreases are mainly due to friction and are smaller than those in the evaporator. As expected, in the condenser section, the pressure and temperature are partially recovered. The degree of recovery for the one with six small PCMs is least due to the larger friction loss.

In Fig. 5, the results shown in Fig. 3 are compared with the results obtained with bigger time step and grid spacings. The time step is increased from 0.1 s to 0.5 s and the grid spacings Δr, Δr_t, and Δz are doubled. As we can see, with bigger time step and coarser grid mesh, the solution still remain almost the same. In other words, the numerical results presented in Fig. 3 are quite independent of time step and grid spacings.

Shown in Figs. 6 and 7 are the transient response of the heat pipes with a pulse heat load applied to the evaporator from $t = 10$ s to $t = 100$ s. As we can see in Fig. 6, the heat pipe responds very fast and the temperature starts to decrease as soon as the pulse heat load is removed at $t = 100$ s. The temperature of the heat pipe without PCM decreases very rapidly after the pulse heat load is removed. The temperatures of the other two with PCMs also decrease rapidly right after this moment, but the decreases become very slow when the PCMs reach the melting point and start to solidify. The six small PCMs are completely solidified earlier than the one big PCM does. After the PCMs are completely solidified, the temperatures of both heat pipes with PCM decrease again and the heat pipes return to the initial steady state condition with $q = 4.3$ W/cm^2. It takes about 1620 s for the heat pipe with six PCMs and about 1740 s for the one with one big PCM to return to the initial steady-state condition after the pulse heat load is removed. Figure 7 shows the percentage of PCMs

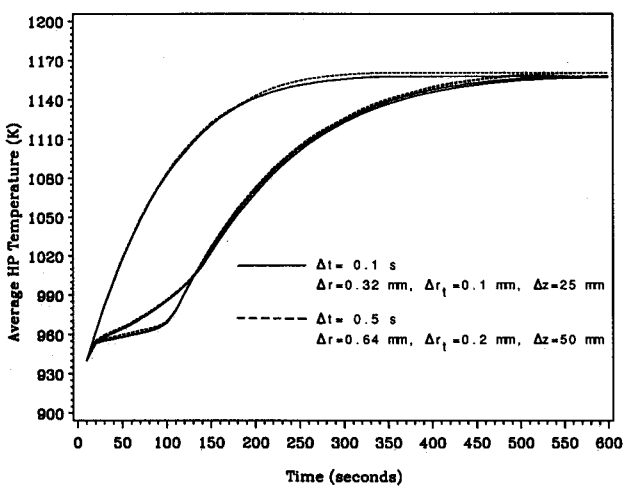

Fig. 5 The dependence of the numerical solutions on time step and grid spacing.

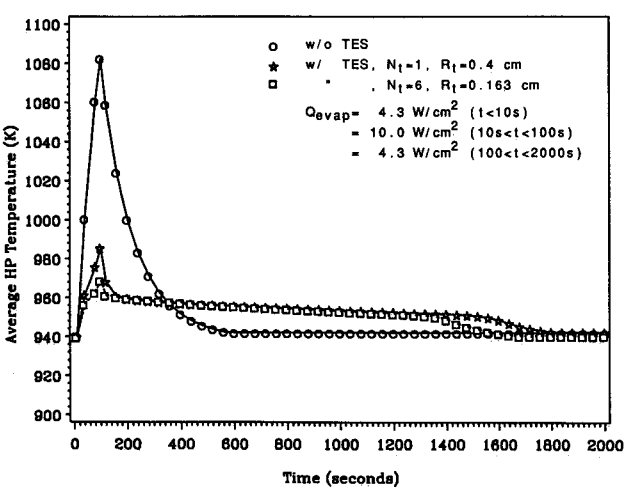

Fig. 6 Transient response of heat pipes with pulse heat load.

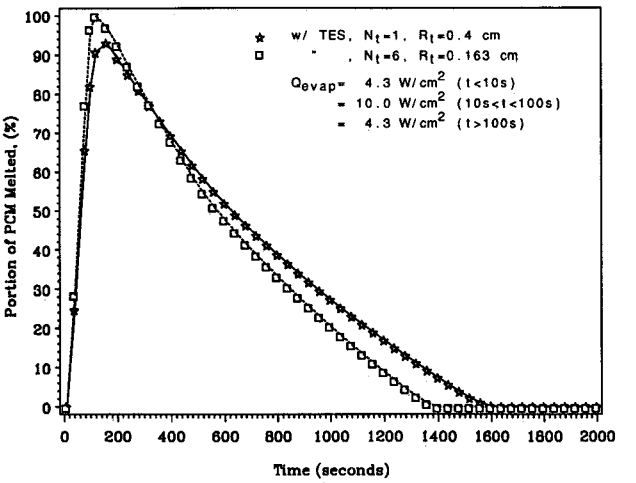

Fig. 7 Portion of PCM melted vs time for pulse heat load.

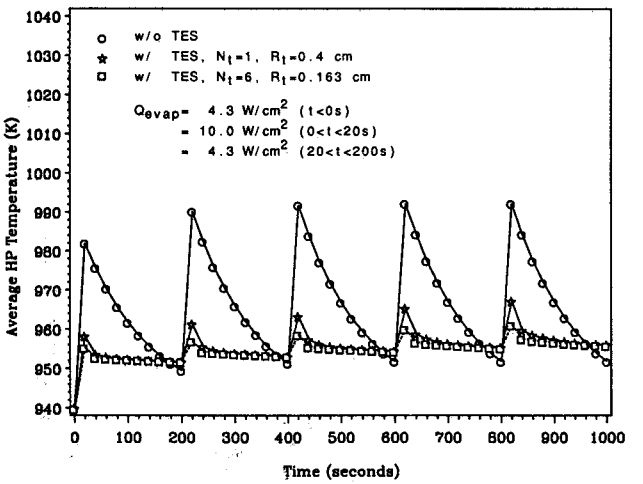

Fig. 8 Transient response of heat pipes with periodic pulse heat loads.

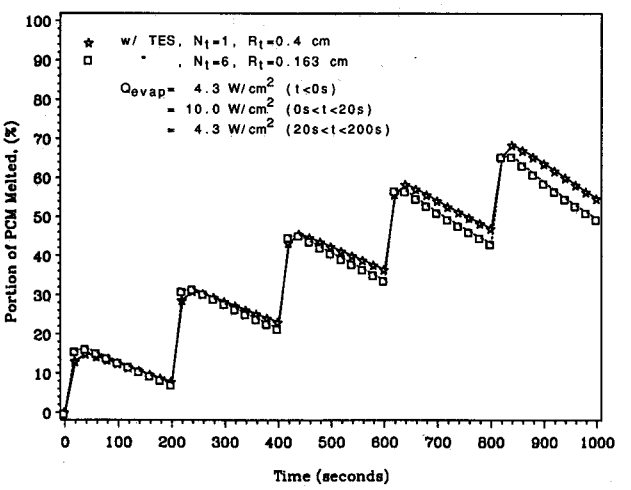

Fig. 9 Portion of PCM melted vs time for periodic pulse heat loads.

melted versus time for the same case shown in Fig. 6. We can see that the PCMs do not respond as fast as the heat pipe temperature does. In fact, after the pulse heat load is removed at $t = 100$ s, 2% more of the six small PCMs and 10% more of the one big PCM continue to be melted. It can also be seen that the small PCM solidifies faster than the big one does.

Figures 8 and 9 show the results of the transient response of the heat pipes with periodic pulse heat loads. The time period is 200 s and each of the pulse heat loads lasts 20 s.

The periodic pulse heat loads are applied before the heat pipes have enough time to return to the inital steady-state condition. The temperature response in each time period is similar to the results shown in Fig. 6. The temperature of the heat pipe without PCM goes up and down periodically. The temperature of the heat pipe with six small PCMs remains also constant throughout the whole duration due to very efficient melting and solidification. As shown in Fig. 9, the percentages of PCM melted for both heat pipes with PCM continue to increase with more and more pulse periods. This is because that the PCMs do not have enough time during the low-power periods to solidify completely at the end of each time period.

The main disadvantage of installing phase-change material in the vapor core of a heat pipe is that the vapor flow area is decreased. The decrease in the vapor flow area can cause the vapor pressure to drop and vapor velocity to increase. However, these increases can be reduced after the PCM starts to melt and absorb a portion of the heat loads. The increases in the vapor pressure drop and vapor velocity depend strongly on how efficiently the PCM can absorb the heat. For a heat pipe operating near its sonic limit (which usually occurs with a liquid metal heat pipe operating at low temperatures when the vapor density is low), the reduction in vapor flow area can pose a severe problem. However, if a heat pipe is already operating at a sufficiently high temperature, the vapor flow usually does not play an important role in determining the heat pipe capability. Then, the increases in the vapor pressure drop and vapor velocity caused by the reduction in vapor flow area would not have a significant effect on the heat pipe capability. In this latter case, the incorporation of phase-change material inside the heat pipe is very effective in mitigating the temperature excursion when the heat pipe is subjected to a pulse load.

The concept of incorporating phase-change material inside a low-temperature heat pipe (such as a water heat pipe) is also sound if the goal is to limit the temperature excursion when the heat load is time dependent. In such a case, we should choose a PCM with a melting point somewhat higher than the normal operating temperature but lower than the maximum allowable heat pipe temperature. To reduce the chance of complete melting of the PCM during the pulse period, the latent heat of fusion of the PCM should be as large as possible.

Conclusions

In this paper, the transient behavior of a high-temperature axially grooved heat pipe with thermal energy storage was modeled. A phase-change material encapsulated in cylindrical containers was used as TES. It was found that the PCM is very effective in mitigating the adverse effect of pulse heat loads on normal heat pipe operation. We also showed that the vapor pressure and temperature drops are strongly dependent on the operating vapor temperature.

Acknowledgment

This work is supported by the Wright Research and Development Center, Contract F33615-87-C-2777.

References

[1]Beam, J. E., Air Force Patent on Reservoir Heat Pipe, 1986.

[2]Sheffield, J. W., "Weight Characteristics of Future Spacecraft Thermal Management Systems," Air Force Technical Rept. AFWAL-TR-84-2005, Feb. 1984.

[3]Chang, M. J., Chow, L. C., and Chang, W. S., "Improved ADI Method for Solving Transient 3-D Heat Diffusion Problems," *Numerical Heat Transfer,* Part B, Vol. 19, 1991, pp. 69–84.

[4]Douglas, J., "Alternating Direction Methods for Three Space Variables," *Numerische Mathematik,* Vol. 4, 1962, pp. 41–63.

[5]Brian, P. L. T., "A Finite-Difference Method of Higher-Order Accuracy for the Solution of Three-Dimensional Transient Heat Conduction Problems," *AIChE Journal,* Vol. 7, 1961, pp. 367–370.

[6]Bowman, W. J., "Simulated Heat Pipe Vapor Dynamics," Ph.D. Dissertation, Air Force Inst. of Technology, 1987.

[7]Hall, M. L., and Doster, J. M., "Transient Thermohydraulic Heat Pipe Modeling," *Fourth Symposium on Space Nuclear Power Systems,* Albuquerque, NM, Jan. 1987.

[8]Kelly, J. M., and Schor, A. L., "Heat Pipe Transient Analysis: Vapor Dynamics," *Fifth Symposium on Space Nuclear Power Systems,* Albuquerque, NM, Jan., 1988.

[9]Issacci, F., Catton, I., Heiss, A., and Ghoniem, N. M., "Analysis of Heat Pipe Vapor Dynamics," *American Society of Mechanical Engineers,* National Heat Transfer Conf., Houston, Texas, July 1988.

[10]Hsiao, J. S., "An Efficient Algorithm for Finite-Difference Analysis of Heat Transfer with Melting and Solidification," *Numerical Heat Transfer,* Vol. 8, 1985, pp. 653–666.

[11]Pham, Q. T., "An Fast, Unconditionally Stable Finite-Difference Scheme for Heat Conduction with Phase Change," *International Journal of Heat and Mass Transfer,* Vol. 28, No. 11, 1985, pp. 2079–2084.

[12]Pham, Q. T., "A Note on Some Finite-Difference Methods for Heat Conduction with Phase Change," *Numerical Heat Transfer,* Vol. 11, 1987, pp. 353–359.

[13]Barantsevich, V. L., Opryshko, S. I., and Sasin, V. Y., "Methods for Improving the Maximum Heat Transfer Capacity of Axially Grooved Heat Pipes," *Heat Transfer-Soviet Research,* Vol. 16, No. 4, 1984, pp. 92–98.

[14]Thibault, J., "Comparison of Nine Three-Dimensional Numerical Methods for the Solution of the Heat Diffusion Equation," *Numerical Heat Transfer,* Vol. 8, 1985, pp. 281–298.

[15]Patankar, S. V., *Numerical Heat Transfer and Fluid Flow,* McGraw Hill, New York, 1980, p. 37.

[16]Morris, D. G., Foote, J. P., and Olszewski, M., "Development of Encapsulated Lithium Hydride Thermal Energy Storage for Space Power Systems," Oak Ridge National Laboratory (ORNL)/TM-10413, Dec. 1987.

[17]Shapiro, A. H., *The Dynamics and Thermodynamics of Compressible Fluid Flow,* Vol. 1, Ronald Press Co., New York, 1953, pp. 238–241.